Check for updates

Massively parallel functional photoacoustic computed tomography of the human brain

Shuai Na [1,9], Jonathan J. Russin[2,3,4,9], Li Lin [1,9], Xiaoyun Yuan[1,7,9], Peng Hu [1], Kay B. Jann[5], Lirong Yan[5], Konstantin Maslov[1], Junhui Shi[1,8], Danny J. Wang [5], Charles Y. Liu [2,3,4 ✉] and Lihong V. Wang [1,6 ✉]

Blood-oxygen-level-dependent (BOLD) functional magnetic resonance imaging of the human brain requires bulky equipment for the generation of magnetic fields. Photoacoustic computed tomography obviates the need for magnetic fields by using light and sound to measure deoxyhaemoglobin and oxyhaemoglobin concentrations to then quantify oxygen saturation and blood volumes. Yet, the available imaging speeds, fields of view (FOV), sensitivities and penetration depths have been insufficient for functional imaging of the human brain. Here, we show that massively parallel ultrasonic transducers arranged hemispherically around the human head can produce tomographic images of the brain with a 10-cm-diameter FOV and spatial and temporal resolutions of 350 μm and 2 s, respectively. In patients who had a hemicraniectomy, a comparison of functional photoacoustic computed tomography and 7 T BOLD functional magnetic resonance imaging showed a strong spatial correspondence in the same FOV and a high temporal correlation between BOLD signals and photoacoustic signals, with the latter enabling faster detection of functional activation. Our findings establish the use of photoacoustic computed tomography for human brain imaging.

Since its inception in 1990, blood-oxygen-level-dependent (BOLD) imaging—the primary form of functional magnetic resonance imaging (fMRI)—has been the mainstay of non-invasive brain function imaging[1,2]. A state-of-the-art 7 T MRI system can achieve a sub-millimetre/sub-second spatiotemporal resolution but weighs over 20 ton and costs more than US$6 million[3,4]. Moreover, MRI is contraindicated in some patients with ferromagnetic implants or claustrophobia and can be difficult to tolerate due to the loud operation noise[5,6]. Alternatively, nuclear-based neuroimaging approaches can image neurometabolism, but they generally have poor temporal resolutions and are limited by the use of radioactive isotopes[7]. Electroencephalography, magnetoencephalogram and functional near-infrared spectroscopy can provide high temporal resolutions but have poor spatial resolutions and lack anatomical information[8,9]. Although functional ultrasound has been demonstrated in human neonatal brains through fontanelles, it is limited to a relatively small coronal field of view (FOV) and is insensitive to blood flows parallel to the probe surface due to the angle dependence of the Doppler effect[10].

Photoacoustic (PA) computed tomography (PACT) reconstructs the vasculature non-invasively using acoustic waves stemming from the optical absorption of endogenous haemoglobin (Hb) and can therefore image neuroactivities on the basis of neurovascular coupling[11]. In contrast to BOLD fMRI, PACT is directly sensitive to both deoxyhaemoglobin (HbR) and oxyhaemoglobin (HbO₂). The linear relationship of their distinct spectral signatures enables the quantification of both concentrations and conversion to oxygen saturation (sO₂) and cerebral blood volume (CBV)[12]. In the last two decades, PACT has been explored in angiology, oncology, gastroenterology, cardiology and neurology[11-21]. However, PACT of the human brain has not yet been achieved. Previously described panoramic two-dimensional (2D) PACT systems could not discriminate between signals originating from the brain and overlying tissues due to the lack of elevational resolution[11,22]. Furthermore, previously described 3D systems were either too slow to overcome motion artifacts and capture fast functional signals or insufficiently sensitive to detect subtle haemodynamic changes[23-26]. In this Article, we report an in vivo 3D functional human brain PACT system of 1,024 (1K) parallel ultrasonic transducer elements, termed 1K3D-fPACT. Functional imaging was performed in patients who had a hemicraniectomy by replicating landmark fMRI tasks of motor function and language. The recorded functional activation was validated against 7 T fMRI results and self-verified by repeated measurements. We also imaged a patient with metal implants and demonstrated the use of 1K3D-fPACT in populations in which MRI was not well tolerated. Collectively, in its infancy, the proposed technology demonstrates comparable results to the current gold standard for imaging human brain vasculature and function.

Results

The 1K3D-fPACT system. The design of the 1K3D-fPACT centres around the challenges associated with FOV, sensitivity, spatiotemporal resolution, functional contrast, ergonomic head support and motion control. As shown in Fig. 1a,b, the 1K3D-fPACT consists of five main parts—a dual-wavelength (1,064 nm and 694 nm) laser module to excite PA waves with both HbO₂ and HbR

[1]Caltech Optical Imaging Laboratory, Andrew and Peggy Cherng Department of Medical Engineering, California Institute of Technology, Pasadena, CA, USA. [2]Department of Neurological Surgery, Keck School of Medicine, University of Southern California, Los Angeles, CA, USA. [3]Neurorestoration Center, Keck School of Medicine, University of Southern California, Los Angeles, CA, USA. [4]Rancho Los Amigos National Rehabilitation Center, Downey, CA, USA. [5]Laboratory of Functional MRI Technology, Stevens Neuroimaging and Informatics Institute, Keck School of Medicine, University of Southern California, Los Angeles, CA, USA. [6]Caltech Optical Imaging Laboratory, Department of Electrical Engineering, California Institute of Technology, Pasadena, CA, USA. [7]Present address: Department of Electronic Engineering, Tsinghua University, Beijing, China. [8]Present address: Zhejiang Lab, Hangzhou, China. [9]These authors contributed equally: Shuai Na, Jonathan J. Russin, Li Lin, Xiaoyun Yuan. ✉e-mail: cliu@usc.edu; LVW@caltech.edu
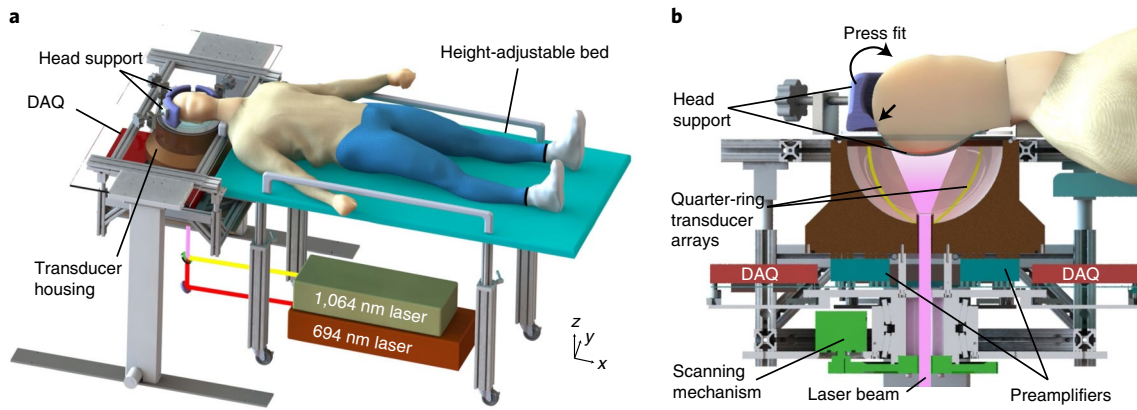
Fig. 1 | Representations of the 1K3D-fPACT. a, Perspective view of the system. **b**, Perspective cut-away view of the imager.

contrasts; four 256-element quarter-ring ultrasonic transducer arrays evenly distributed on a hemispherical bowl to record PA signals panoramically; a one-to-one mapped signal amplification and data acquisition (DAQ) system to amplify and digitize the PA signals; a scanning mechanism to provide azimuthal samplings; and a head support and a height-adjustable bed to stabilize the head ergonomically (details of the system design and construction are provided in the Methods). The system schematic and infrastructure are shown in Supplementary Figs. 1 and 2. The 1K3D-fPACT is operated using custom software that enables dual scanning modes—baseline and function. Measurement starts with the baseline mode to acquire brain angiography followed by the functional mode to image brain function. The data acquisition and laser control methodologies are described in the Methods and Supplementary Fig. 3. Presently, the 1K3D-fPACT provides a 10-cm-diameter FOV on the head, an isotropic spatial resolution of 350 μm, and a temporal resolution of 10 s for the baseline mode and 2 s for the functional mode. However, the 1K3D-fPACT is scalable in terms of imaging rate and FOV (Methods). The >20,000 (at 1,064 nm) and >2,000 (at 694 nm) detector positions distributed on a hemisphere formed by each one-way functional scan enable the system to retain a detectability of ~2% Hb signal change for 1,064 nm and ~6% Hb signal change for 694 nm up to ~11 mm below the cortical surface or ~20 mm from the skin surface—deep enough to image the entire cortical thickness of the cerebral gyri[27] (the characteristics of the system performance are shown in Supplementary Fig. 4).

Brain angiography. Empowered with a high spatiotemporal resolution and sensitivity, the 1K3D-fPACT can image both brain function and angiographic structures, facilitating coregistration between the fPACT and fMRI results. Brain angiography was performed in four post-hemicraniectomy participants using both the 1K3D-fPACT and 7 T magnetic resonance angiography (MRA) (details about the participants are provided in the Methods). Considering the larger absorption coefficient of HbO_2 at 1,064 nm, the baseline images acquired at 1,064 nm were used to evaluate the PACT angiography. The MRA was acquired using a time-of-flight (TOF) sequence that provided an isotropic spatial resolution of 0.4 mm (Methods). For comparison, the 3D MRA and PACT images were first segmented into scalp and cortical regions on the basis of the cortical contours. The MRA images were then truncated to preserve all vessels within 4 cm of the scalp surface. The segmented scalp and cortical vasculatures were individually coregistered (Supplementary Fig. 5) and presented as maximum amplitude projections (MAPs) in Fig. 2a–d. The 1K3D-fPACT angiography and MRA result in a strong visuo-spatial correlation (Supplementary Videos 1 and 2). Vessel pattern discrepancies are attributable to two reasons. First, the MRA TOF

sequence detects inflow effects, which are sensitive only to arteries. By contrast, PACT is sensitive to Hb and images both arteries and veins. Second, as PACT and MRA were conducted non-concurrently and in different participant positions (lateral decubitus versus supine), spatial discrepancies could arise from tissue deformation, exacerbated by the craniectomy, and errors in spatial co-registration between modalities. Quantitively, the measured vasculature diameters of participant 1 exhibit a strong agreement (Fig. 2e). Although we used the angiographic results mainly for coregistration and comparisons, the potential of the 1K3D-fPACT to diagnose cerebral vascular diseases is evident.

Mapping motor function. Three block-designed motor tasks—sequential finger tapping (FT), lip puckering (LP) and tongue tapping (TT), were imaged using the 1K3D-fPACT and 7 T fMRI (see the Methods for protocols, Supplementary Fig. 6 for stimulation paradigms and Supplementary Video 3 for the experimental video). Functional responses to these tasks have been demonstrated to involve anatomically proximate cortical regions that require a high spatial resolution to differentiate[28]. For both modalities, brain activities were extracted for each voxel on the basis of its absolute value fluctuation using the general linear model (GLM)[29] (Methods and Supplementary Methods 1). The functional maps were registered to the T1-weighted cortical images on the basis of a systematic coregistration framework (Supplementary Fig. 5) and presented in Fig. 3a–h (comparisons of the results between modalities are shown in Supplementary Videos 1 and 2). The goodness of fit of the GLM was examined using the *F*-test (Supplementary Fig. 7). In Fig. 3i–p, the spatial correspondence between the *t*-maps was assessed using three metrics—dice coefficient (DC), spatial correlation (SC) and centre-of-mass error (CE) (Methods). The DC values ranged from 0.30 to 0.56 for all of the motor tasks, resulting in a fair to moderate agreement. The SC values ranged from 0.29 to 0.47 for all of the motor tasks, resulting in a fair to moderate agreement. The CE values ranged from 0.54 mm to 12.86 mm, demonstrating acceptable CE variations except for TT. Furthermore, we repeated measurements to evaluate the reproducibility of the results when the participants were repositioned on the scanner in separate sessions (Supplementary Fig. 8 and Supplementary Tables 1 and 2). Receiver operating characteristic (ROC) curves were generated on the basis of the data of motor tasks. For each task, the fPACT results of the same task were used as the positive samples, and the fPACT results of the other two tasks were used as the negative samples. fMRI results were used as the gold standards, and SC was chosen as the metric because it was independent of *t*-score thresholding. The ROCs were produced by varying the threshold of SC from −1 to 1. Figure 3q shows the ROC averaged across motor tasks at each
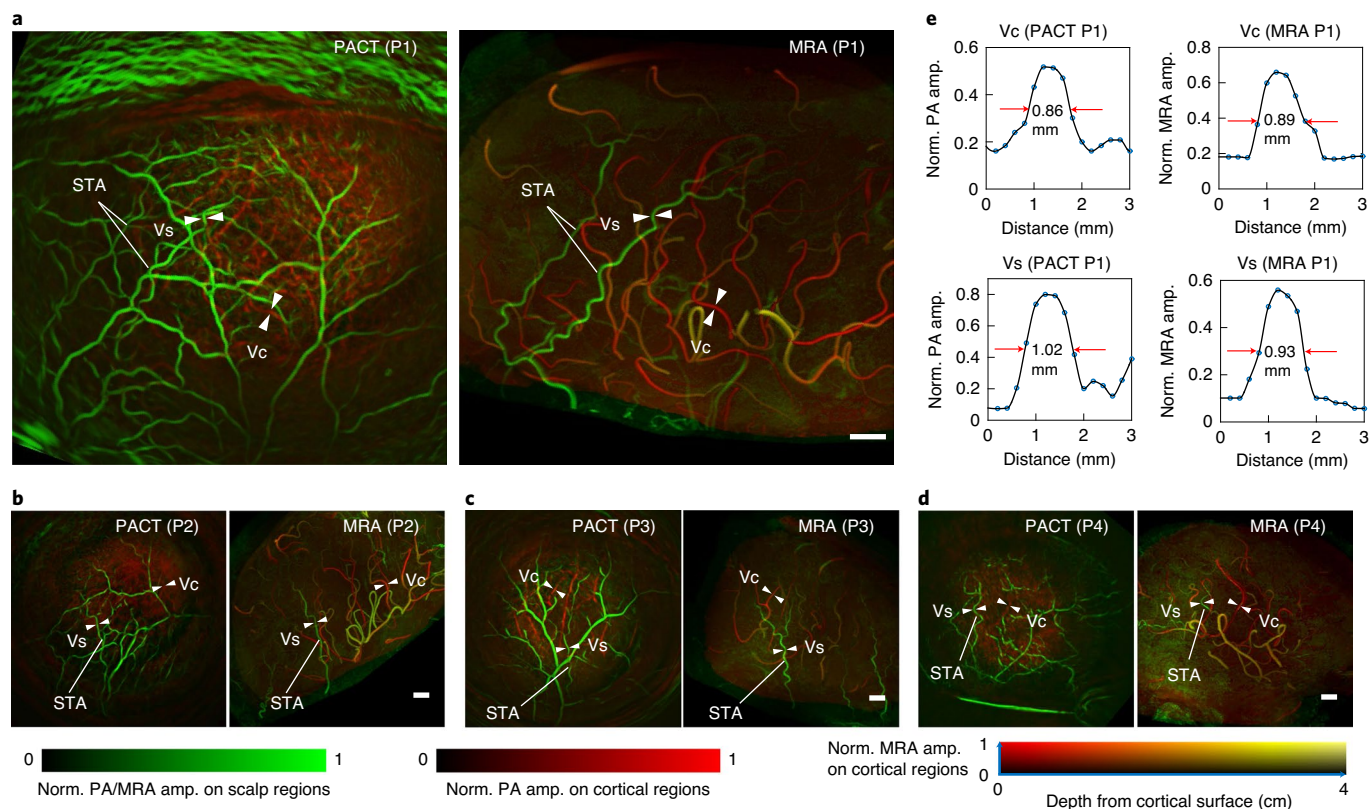
Fig. 2 | PACT angiography and MRA of the same brains. a–d, Vasculatures imaged in participants 1–4 (P1–4; **a–d**, respectively) using the baseline PACT (left) and MRA (right). The images were segmented into the scalp (green) and cortical (red for PACT, 2D colour map for MRA) regions. The scalp and cortical images were normalized to their maximum voxel PA or MRA values (arbitrary units). **e**, The diameters of the selected scalp vessel (Vs) and cortical vessel (Vc) of participant 1 were quantified as the full width at half maximum (red arrows). The y axes represent the voxel amplitudes in **a**. The labelled scalp vessel, cortical vessel and superficial temporal arteries (STA) in **a–d** can be referred to for visuospatial correlation. Norm., normalized; amp., amplitude. For **a–d**, scale bars, 1 cm.

threshold value. A threshold within (0.13, 0.27) produced a sensitivity (true-positive rate) of 83% and specificity (1 – false-positive rate) of 85%–93% (Fig. 3q, solid red line). The average area under the ROC (AUC) was calculated to be 0.94.

We used the FT data as representatives for temporal analysis (Supplementary Fig. 9a,b). Figure 3r shows the mean fractional changes of BOLD and PA signals over stimulation cycles averaged across participants. The concentration fractional changes of Hb species are shown in Fig. 3s (Supplementary Methods 2). The changes in total Hb (HbT) concentration also reflect the local blood volume changes as they are proportional. As the reciprocal of BOLD signals acquired with gradient echo correlate well with HbR, we used 1/BOLD to correlate with the concentration fractional changes of Hb species and observed a strong correlation[30] (Fig. 3t). As the optical absorptions of HbO_2 and HbR are dominant at 1,064 nm and 694 nm, respectively, the fractional changes of 1/BOLD and PA signals also establish a strong correlation ($r = 0.89$ for 1,064 nm and $r = 0.96$ for 694 nm; Supplementary Fig. 9c). Figure 3u shows the relative changes of sO_2 averaged across participants demonstrating a ~1% sO_2 relative change. Repeated measurements in separate sessions show reproducible temporal responses (Supplementary Fig. 10). We compared the response speeds of BOLD and PACT-derived signals in response to stimulations. The onset time, defined as the time to 50% peak (>2 s.e.m. at $t = 0$), was found to be 7.8 ± 0.6 s for BOLD, 6.5 ± 0.6 s for sO_2 and 6.1 ± 0.7 s for HbT (mean ± s.d., $n = 4$ participants), demonstrating that the 1K3D-fPACT can detect function faster than BOLD fMRI ($P = 0.039$ for BOLD and sO_2; $P = 0.022$ for BOLD and HbT; paired

one-sided Student's t-tests) due to its diverse functional contrasts (Supplementary Fig. 9d). We define the contrast-to-noise ratio (CNR) of the functional signals as $CNR = S/\text{s.e.m.}$, where S is the mean of the absolute contrasts between the signal peaks and the baselines over stimulation cycles. Figure 3v shows that the average CNR of the PA signals at 1,064 nm is lower but comparable to that of BOLD signals. Due to fewer scanning angles, the CNR of the PA signals acquired at 694 nm is relatively lower yet has an average value greater than two.

Mapping language areas. To evaluate the 1K3D-fPACT for mapping different aspects of language-evoked brain function, we used passive story listening (PL) and silent word generation (WG) tasks to isolate the sensory and semantic aspects of language function (see the Methods for protocols and Supplementary Fig. 6 for stimulation paradigms). In Fig. 4, functional maps from fPACT and fMRI were extracted and coregistered to the T1-weighted cortex following the same data processing routines (Supplementary Methods 1). For both fMRI and fPACT, the WG results show a relatively broad area of activation, which largely corresponds to Broca's area. Broca's area is predominantly located in the left hemisphere[31], and our results are consistent with this fact, given that results from participants 1 and 2 demonstrated strong activation, whereas the right hemisphere of participant 3 showed less notable activation (Fig. 5d; cross-modality comparisons of the functional results are shown in Supplementary Videos 1 and 2). The DC values of 0.41 and 0.50, and SC values of 0.33 and 0.51 result in a fair to moderate agreement for PL. The smaller DC values for WG are most likely attributable
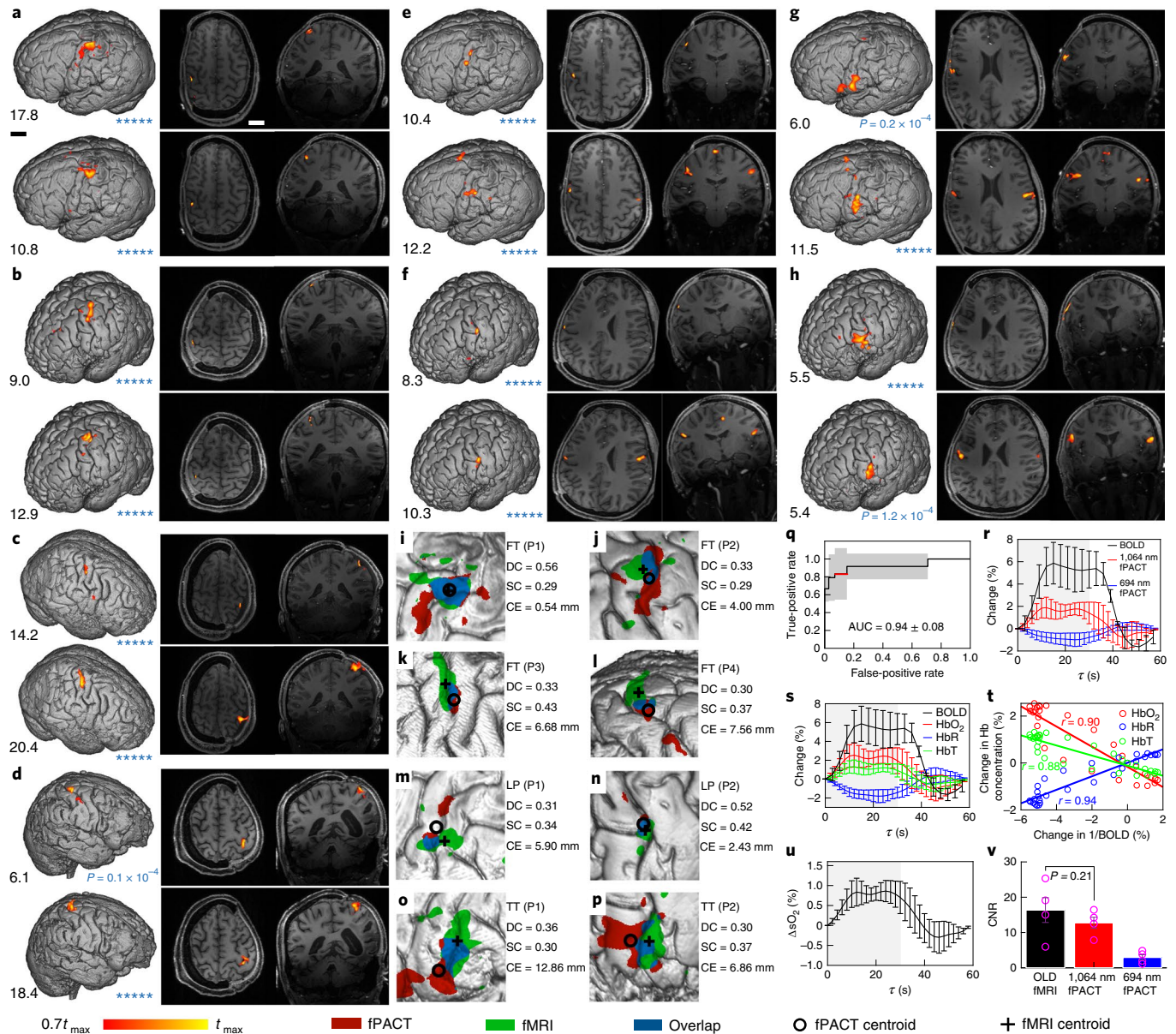
Fig. 3 | Evaluating the 1K3D-fPACT for brain function mapping using 7 T fMRI and motor tasks. a–h, Functional responses to FT were recorded in participants 1–4 (**a–d**, respectively), and responses to LP (**e,f**) and TT (**g,h**) were acquired in participant 1 (**e,g**) and participant 2 (**f,h**). The fPACT and fMRI results are displayed in the first and second rows, respectively. Each functional map reflects the *t* values of greater than 70% of the maximum. The maximum *t* value (black) is shown below the cortex. The *P* value corresponding to 70% of the maximum *t* value is displayed (blue) below the cortex. Statistical analysis was performed using one-sample one-sided Student's *t*-tests; *****$P < 0.00001$ (d.f. = 222 for fPACT, d.f. = 142 for fMRI, no adjustment; *q* (FDR-adjusted *P* values) < 0.05 for all maps). The functional maps displayed on the cortex represent MAPs of the responses within a 2 cm depth. Functional distributions are displayed on the axial (middle column) and coronal (right column) brain slices that pass the midpoints of the line connecting the centroids of the activated maps of both modalities. FT, LP and TT were measured three times for participant 1 and once for participant 2; FT was measured twice for participants 3 and 4 (Supplementary Fig. 8). Scale bars, 2 cm; the scale bars in **a** also apply to the respective images in **b**–**h**. **i–p**, The functional maps of FT, LP and TT for participant 1 (**i–k**, respectively), of FT, LP and TT for participant 2 (**l–n**, respectively), and of FT for participants 3 and 4 (**o,p**, respectively) were compared on the basis of the DC, SC and CE in a 4×4 cm² FOV. The binarized functional maps used in the DC calculation are shown. **q**, ROC averaged across $n = 3$ motor tasks at each threshold value. Data are mean ± s.d. **r**, Measured fractional changes of the BOLD and PA signals during the FT task. Data are mean ± s.d. $n = 4$ participants. The grey area represents the stimulation period. **s**, Calculated concentration fractional changes for each Hb species. Data are mean ± s.d. $n = 4$ participants. **t**, The concentration fractional changes of each Hb species versus 1/BOLD fractional changes. **u**, The relative changes of sO₂ during FT. Data are mean ± s.d. $n = 4$ participants. **v**, CNRs of BOLD and PA signals. Data are mean ± s.e.m. $n = 4$ participants. The *P* value was computed using a paired two-sided Student's *t*-test. *τ*, time.

to the thresholding-induced discontinuity in the activated clusters because the SCs implicate a better agreement. The CE values range from 4.87 mm to 7.00 mm, demonstrating acceptable localization

discrepancies. Repeated measurements also demonstrated good repeatability of the functional results (Supplementary Fig. 8 and Supplementary Tables 1 and 2).
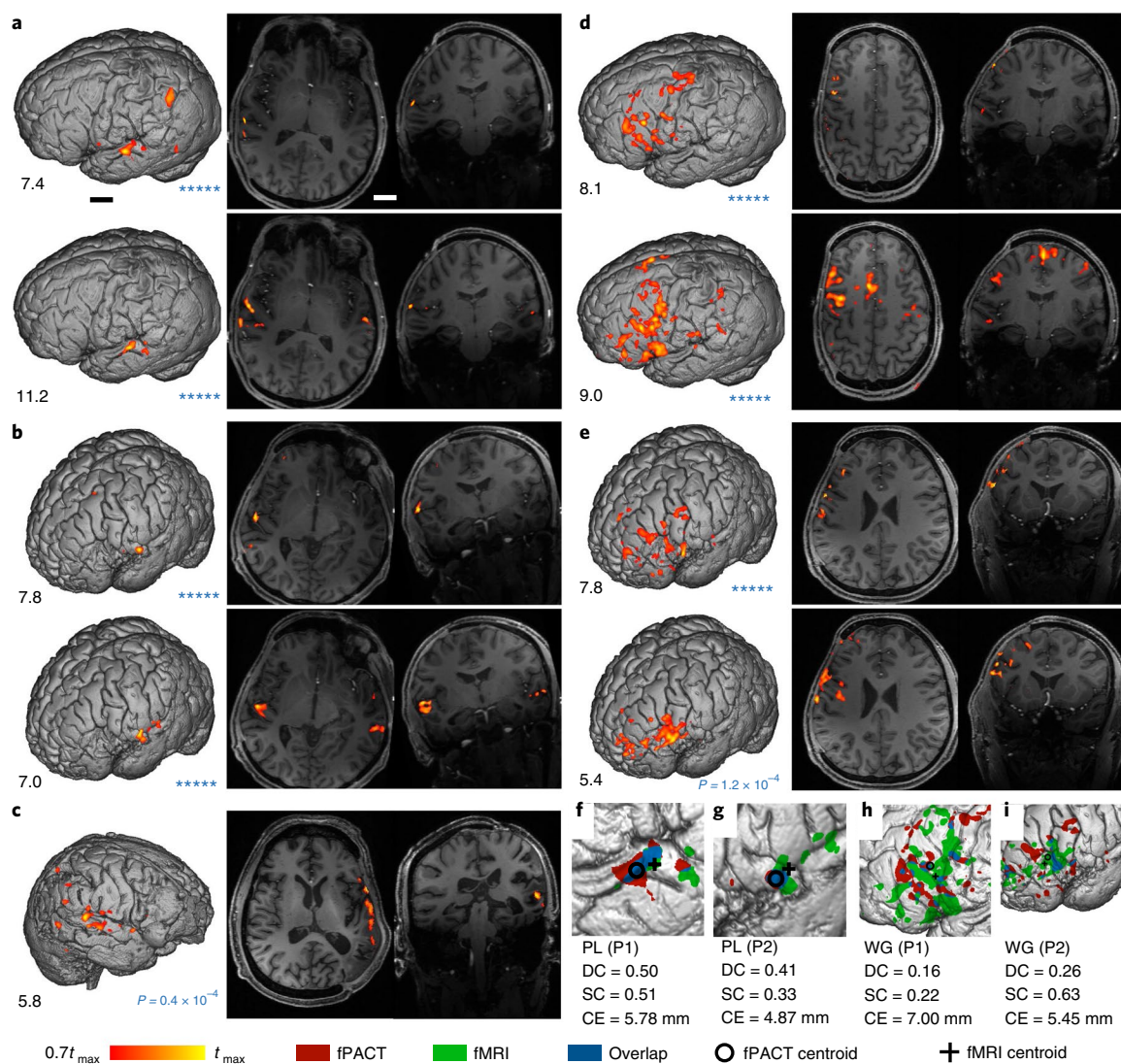
Fig. 4 | Imaging language processing. a–e, Functional responses to PL (**a–c**) and WG (**d,e**) were recorded in participant 1 (**a,d**) and participant 2 (**b,e**). The fPACT and fMRI results are displayed in the first and second rows, respectively. Participant 4 underwent PL only in the PACT session (**c**). The maximum t value (black) is displayed below the cortex. The P value corresponding to 70% of the maximum t value is displayed (blue) below the cortex. Statistical analysis was performed using one-sample one-sided Student's t-tests; *****$P < 0.00001$ (d.f. = 207 for fPACT, d.f. = 132 for fMRI, no adjustment; $q < 0.05$ for all maps). PL and WG were measured three times for participant 1 and once for participant 2; PL was measured twice for participant 4 (Supplementary Fig. 8). Scale bars, 2 cm; the scale bars in **a** also apply to the respective images in **b–e**. **f–i**, The binary masks of the responses are displayed in a FOV of $4 \times 4\,cm^2$ for PL (**f,g**) and $10 \times 10\,cm^2$ for WG (**h,i**) for participant 1 (**f,h**) and participant 2 (**g,i**). For participant 4, the PL responses fall into the auditory cortex regions, which topographically agrees with those observed in the other participants.

Mapping brain function in a participant with implants.
Participant 3 required metal implants for the treatment of an orthopaedic injury sustained in conjunction with the head trauma. The implants were cleared for 7 T; however, discomfort at the implant site during fMRI acquisition was substantial enough to require abortion of the scan. As a consequence, only T1-weighted MRI, MRA and fMRI of FT were acquired. Implants are not uncommon in patients who have had a craniectomy due to the polytraumatic nature of many traumatic brain injuries (for example, implanting fixation plates at fracture sites). Due to the non-invasive and magnet-free nature of the 1K3D-fPACT, all functional studies were attained in participant 3 without reported issues. Although fMRI results were lacking, the functional responses to LP, TT, and PL recorded by the 1K3D-fPACT exhibit topographies comparable to those obtained in the other participants (Figs. 3 and 4) and the previously reported results[32,33]. In Fig. 5d, the less notable and

non-reproducible responses to WG are attributable to the fact that the right hemisphere is not the dominant hemisphere for language[31] (Supplementary Fig. 8 and Supplementary Table 2). By contrast, the fMRI and fPACT results of participants 1 and 2 showed substantial responses in the left hemispheres as indicated in Fig. 4d,e, and repeated measurements in Supplementary Fig. 8a,b. Thus, the WG data of participant 3 (Fig. 5d and repeated measurements in Supplementary Fig. 8c) can be considered to be a negative control. The anatomical and functional results of participant 3 are displayed in Supplementary Video 2.

Discussion
This study demonstrated PACT technology in imaging human brain function. We used motor tasks to evaluate the ability of the 1K3D-fPACT to discriminate between anatomically proximate areas, and the language protocols to image distributed brain activities.
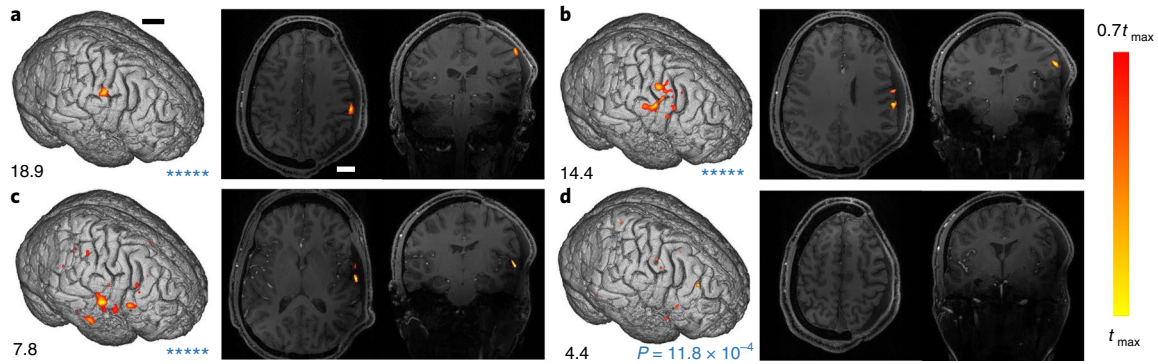
Fig. 5 | Measuring brain function in a participant who experienced discomfort in MRI due to implants. a–d, Functional responses recorded by the 1K3D-fPACT during LP (**a**), TT (**b**), PL (**c**) and WG (**d**). The maximum t value (black) is displayed below the cortex. The P value corresponding to 70% of the maximum t value is displayed (blue) below the cortex. Statistical analysis was performed using one-sample one-sided Student's t-tests; *****$P < 0.00001$ (d.f. = 222 for fPACT LP and TT, d.f. = 207 for fPACT PL and WG, d.f. = 142 for fMRI LP and TT, d.f. = 132 for fMRI PL and WG, no adjustment; $q < 0.05$ for all maps). LP, TT, PL and WG were measured twice (Supplementary Fig. 8). Scale bars, 2cm; the scale bars in **a** also apply to the respective images in **b**–**d**.

Table 1 | Strengths of the 1K3D-fPACT over BOLD fMRI for cortical neuroimaging

Modality	Contrast	Response	Background	Sensitivity	Linearity	Portability	Space	Sound	Costs	Magnet
fMRI	HbR	Early	High	Low	No	No	Closed	Loud	High	Yes
fPACT	HbR, HbO$_2$, sO$_2$, CBV	Earlier	Low	High	Yes	Yes	Open	Quiet	Low	No

The functional results demonstrate a ~1 cm depth from the cortical surface and are quantitively comparable to those obtained with 7 T fMRI. Discrepancies are attributable to the following factors. First, experiments of fPACT and fMRI were non-concurrent, leading to physiological variations. Second, tissue deformation induced by different imaging postures of the two modalities introduced coregistration errors. Third, although it is the current gold standard, fMRI still has limitations regarding sensitivity and specificity for functional imaging.

Here, the radiant exposure on the skin was ~23 mJ cm^{-2} for 1,064 nm, approximately 1/4 of the American National Standards Institute (ANSI) limit[34] (100 mJ cm^{-2}; Methods). If the radiant exposure is increased to the ANSI limit, we expect to detect function at a greater depth of ~2.3 cm, at which the current detectability is ~8% (Supplementary Fig. 4c). Compared with MRI, the 1K3D-fPACT is presently limited to imaging the superficial cortex. However, it can potentially monitor the resting-state dynamics in at least portions of all of the major networks through their nodes in the cortex[35].

Although the unique hemicraniectomy population provides an acoustic window enabling aberration-free image reconstruction, transcranial PACT is potentially achievable. For transcranial PACT, the signal-to-noise ratio (SNR) is compromised by the skull-induced optical attenuation and acoustic aberration (including acoustic attenuation and wavefront distortion). Our preliminary studies have shown that an adult human skull induces ~50% light attenuation at 1,064 nm and ~80% acoustic pressure attenuation[36]. Given the SNR of ~50 achieved at ~11 mm below the cortical surface in patients who had a hemicraniectomy, the SNR for transcranial PACT at the same cortical depth would decrease to ~5. To detect the functional change of typically several percent, further improvement is required. First, a system with a lower centre frequency (for example, 1 MHz) is desired because the skull-induced acoustic attenuation is frequency dependent, and the transcranial PA signal centres at ~0.75 MHz (ref. [36]). As the dimension of an ultrasonic transducer element is inversely proportional to its centre frequency for a given acceptance angle, the dimension of a 1 MHz transducer element should be 2.1 times that of the current system, improving the SNR by 2.1 times. Second, if the radiant exposure is increased to the ANSI limit, the SNR can be improved by a factor of ~4. Third, given that the current element count can be tripled, the SNR can gain another factor of $\sqrt{3}$. With the above potential improvement, we expect the transcranial detectability to be ~1.4% at ~1 cm below the cortical surface. The recent improvement in ultrasonic transducer sensitivity can also potentially enhance the SNR of transcranial PACT[37]. However, note that the estimated SNR above assumed that there was no skull-induced acoustic distortion. State-of-the-art deaberration techniques are mainly based on full-wave acoustic modelling and the assumption of homogeneous skull acoustic properties. The current challenges are high computational cost and limited reconstruction quality[38–41]. We are developing the next-generation reconstruction algorithms that account for the skull acoustic heterogeneity and incorporate artificial intelligence for speed[42–44].

Table 1 includes relevant comparisons between the 1K3D-fPACT and BOLD fMRI in functional human brain imaging. Fundamentally, the 1K3D-fPACT can quantify the concentrations of both HbO$_2$ and HbR. Other contrasts, including sO$_2$ and CBV, can be derived from the HbO$_2$ and HbR concentrations. The diverse contrasts of the 1K3D-fPACT enable it to detect functional activation faster than BOLD fMRI: 6.1 ± 0.7 s versus 7.8 ± 0.6 s (mean ± s.d., $n = 4$ participants), and potentially with greater specificity. As the system performance evolves, we expect to detect even faster functional activation as demonstrated in small animals[45]. At certain near-infrared wavelengths, PA signals are almost exclusively from Hb species due to their much higher absorption coefficients than other tissue components. This results in excellent sensitivity in detecting Hb with negligible background. By contrast, BOLD fMRI detects neural activities based on only paramagnetic HbR in a nonlinear

relationship with a modest sensitivity due to substantial tissue background. Practically, the 1K3D-fPACT has benefits over MRI in portability, space, operation sound, operation and maintenance costs. Free of strong magnetic fields, the 1K3D-fPACT is also able to obtain functional images in patients with ferromagnetic implants/devices. Similarly, the 1K3D-fPACT will be favourable for introducing neuromodulators and complementary imaging/recording modalities, creating unique clinical and research opportunities. Collectively, the presented results demonstrate that fPACT technology is likely to be a robust, powerful and practical tool for human neuroimaging in future.

Methods

1K3D-fPACT system design and construction. To enrich the functional contrast, two types of Q-switched laser—Nd:YAG (pulse repetition frequency (PRF): 10 Hz, maximum pulse energy: ~2.2 J, pulse width: 8–12 ns) and ruby (PRF: 1 Hz, maximum pulse energy: ~1.7 J, pulse width: 12–20 ns)—are used to enable dual-wavelength contrasts at HbO_2 dominant 1,064 nm and HbR dominant 694 nm. To improve the sensitivity and spatiotemporal resolution, a massively parallel 1,024-element ultrasonic transducer array was designed in the laboratory and custom-built with a 1.5×1.5 mm^2 active element area, 2.4 mm element pitch distance and 2.12 MHz central frequency with a one-way −6 dB bandwidth of 1.73 MHz and a one-way fractional bandwidth of 78% (Supplementary Fig. 4a). The 1,024 elements are evenly distributed in four-quarter rings directly connected to four 256-channel ultra-low-noise preamplifier modules (51 dB gain). The amplified PA signals are digitized by four 256-channel DAQ boards (12 bit dynamic range, 20 MHz sampling rate, 6 dB gain, 7.5 MHz analogue anti-aliasing filter) and streamed to a workstation through USB 3.0 in real time. The four-quarter-ring design enables not only sufficiently dense elevational samplings but also an anatomical scan (400 azimuthal scanning angles) to be completed within a 10 s single-breath-hold period and a functional volumetric imaging rate of 0.5 Hz (80 azimuthal scanning angles at 1,064 nm and 8 azimuthal scanning angles at 694 nm). We chose a customized hemispherical array instead of a commercially available matrix array because the hemispherical configuration offers a panoramic view of the object, providing a larger FOV with a nearly isotropic 3D resolution and substantially reduced limited-view artifacts[46,47]. We preferred one-to-one mapped preamplifiers and DAQs to multiplexing because multiplexing electronics limit data throughput and may introduce noise and crosstalk. The four-quarter rings were manufactured on the inner surface of a 26-cm-diameter polytetrafluoroethylene (PTFE) hemispherical bowl that can both hold the acoustic coupling medium and reflect/recycle the scattered/reflected excitation light. Considering that deuterium oxide (D_2O) has a light absorption coefficient (0.01 cm^{-1}), ten times smaller than that of ordinary water at 1,064 nm (0.1 cm^{-1}) and a similar one (0.006 cm^{-1}) at 694 nm, we used D_2O (sterilized and recycled) as the acoustic coupling medium between the transducers and the head to maximize the light delivery[48]. The spatial resolution, in terms of full width at half maximum of the point spread function, was measured to be 350 μm isotropic in acoustically homogeneous D_2O (Supplementary Fig. 4b). The laser pulses are partially reflected and sampled by a photodiode to correct for energy fluctuations. An engineered diffuser installed at the bottom centre of the bowl transducer is used to homogenize and expand the laser beams to ~10 cm in diameter on the head. Given the light attenuation in the light path, PRF and illumination area, the radiant exposure (~23 mJ cm^{-2} at 1,064 nm and ~19 mJ cm^{-2} at 694 nm) and fluence rate (~230 mW cm^{-2} at 1,064 nm; ~19 mW cm^{-2} at 694 nm; and ~249 mW cm^{-2} at the two wavelengths) are within the ANSI safety limits (100 mJ cm^{-2} and 1,000 mW cm^{-2} at 1,064 nm; 20 mJ cm^{-2} and 200 mW cm^{-2} at 694 nm; and 860 mW cm^{-2} at the two wavelengths)[34]. As designed, the system adopts supine, lateral and prone positions as standard imaging postures. A height-adjustable bed is used to adjust the trunk height relative to the imager for ergonomic comfort. Although the imaging postures optimized the trade-off between comfort and stability, maintaining a stable head position during functional tasks, with acquisition times of approximately 10 min, posed challenges to the head support design. The head support was designed around a hollow PTFE panel that is detachable from the system. A tensioned disposable polyvinylidene chloride film, which was acoustically and optically transparent, was mounted onto the panel to support and constrain the head in the vertical direction. The film also functions as an isolation layer to prevent cross contamination of D_2O among participants. A small amount of distilled water is applied on top of the film to enhance the acoustic coupling between the skin and the film. To constrain the lateral motion, a press-fit head holder with closable fingers designed and custom-made was mounted on the PTFE panel. Finally, three horizontal fasteners were used to push the fingers against the head to introduce more finger–head friction to constrain the rotational motion of the head. The resulting comfort level enabled imaging sessions to last up to 2 h without reported discomfort. The schematic and infrastructure of the 1K3D-fPACT system are shown in Supplementary Figs. 1 and 2.

1K3D-fPACT acquisition. The transducer array was rotated 90° in 100 equiangular steps reciprocally to simultaneously acquire ten densely sampled images at 1,064 nm and ten partially sampled images at 694 nm in 108 s. The laser

interleaving scheme is described in Supplementary Fig. 3. To achieve an equal spatial sampling density to that of the 1,064 nm images, the 694 nm images were merged after correcting for their relative shifts on the basis of coregistration of the ten 1,064 nm images. The functional scan was performed by rotating the array reciprocally over 90° at 0.5 Hz, resulting in a temporal resolution of 2 s. In each one-way scan, there were 20 equiangular acquisition steps for 1,064 nm and two equiangular acquisition steps for 694 nm. The functional volumetric images were reconstructed using the baseline images as constraints to improve the image SNR and reduce the streaking artifacts induced by limited scanning angles (Supplementary Methods 1).

Scalability of the 1K3D-fPACT. The 1K3D-fPACT is scalable in terms of imaging rate and FOV. The current functional scan is configured to 0.5 Hz to balance the spatial sampling density and imaging rate. However, it can be improved by using high-PRF lasers, combining multiple laser sources/increasing the transducer element count. The current FOV (~10 cm in diameter on the head) is limited by the illumination area (proportional to the laser pulse energy with radiant exposure kept constant) and sampling density (proportional to the laser PRF and transducer element count for the same imaging rate). Therefore, improving the laser PRF or element count can enlarge the FOV. However, note that there is an upper limit for the laser RPF defined by the ANSI safety standards described above. The PA amplitude is proportional to the radiant exposure, and therefore the highest radiant exposure, within the safety limit, provides the highest SNR if the image acquisition time is held constant.

7 T MRI acquisition. MRI was collected using a 7 T Siemens Terra scanner (Siemens Medical Solutions) and a Nova Medical 32-channel head coil (Siemens Medical Solutions). The T1-weighted anatomical image was first collected using the Magnetization Prepared Rapid Gradient Echo (MPRAGE) (echo time (TE) = 2.95 ms, repetition time (TR) = 2,200 ms, flip angle (FA) = 7°, $0.7 \times 0.7 \times 0.7$ mm^3 isotropic voxel, FOV = 224 mm, matrix = 320 × 320, 240 slices). Subsequently, a TOF-MRA (TE = 4.67 ms, TR = 12 ms, FA = 20°, $0.4 \times 0.4 \times 0.4$ mm^3 isotropic voxel, 4 slabs, slices per slab = 60 transverse, FOV = 200 mm, matrix = 496 × 496) was acquired. The BOLD fMRI was obtained using a multiband gradient-echo EPI sequence (TE = 22 ms, TR = 3,000 ms, FA = 80°, phase acceleration factor = 5, simultaneous multi-slice = 2, $1.0 \times 1.0 \times 1.0$ mm^3 isotropic voxel, FOV = 192 mm, matrix = 192 × 192, 92 slices). The fMRI data were pretreated with motion correction, spatial smoothing (3 mm full width at half maximum Gaussian kernel, consistent with the fPACT data) and temporal filtration (0.01 Hz high pass, fourth-order Butterworth) before being analysed by the GLM in SPM12 (ref. [49]).

1K3D-fPACT validation with 7 T fMRI. The functional results from both modalities were quantitively compared using DC, SC and CE. The DC measures the normalized intersection between two functional maps using $2(A_{fPACT} \cap A_{fMRI})/(A_{fPACT} + A_{fMRI})$, where A_{fPACT} and A_{fMRI} are the areas of activated regions of interest in the fPACT and fMRI results. The SC evaluates the spatial correspondence without thresholding. The CE characterizes the localization discrepancies by calculating the absolute Euclidian distance between the weighted centres of mass of the activated regions of interest in fPACT and fMRI results. The DC and SC results are classified as 'no agreement' for [−1, 0], 'slight agreement' for (0, 0.2), 'fair agreement' for [0.2, 0.4), 'moderate agreement' for [0.4, 0.6), 'substantial agreement' for [0.6, 0.8) and 'almost perfect agreement' for [0.8, 1][50].

Participants. The study was approved by the institutional review boards of the California Institute of Technology (Caltech), the University of Southern California (USC) and the Rancho Los Amigos National Rehabilitation Center (RLA). Four adult male patients who had a hemicraniectomy (participant 1: left hemicraniectomy, aged 34, not Hispanic or Latino; participant 2: left hemicraniectomy, aged 25, Latino; participant 3: right hemicraniectomy, aged 19, not Hispanic or Latino; participant 4: right hemicraniectomy, aged 41, Latino) with clinically intact neurologic exams and completely healed surgical wounds were recruited from the RLA. PACT was performed at Caltech, and MRI was conducted at the USC. All of the participants had to pass 7 T screening to ensure safe participation. All of the participants agreed to shave their head for efficient light delivery in the PACT sessions. Written informed consent was obtained from all of the participants according to the study protocols. Participants 1, 3 and 4 underwent multiple fPACT sessions to assess the reproducibility of the fPACT results. As a well-established modality, MRI was acquired only once non-concurrently but on the same day with the first PACT session. Participant 3 dropped out of the fMRI session after the T1-weighted MRI, MRA and FT fMRI was obtained. Participant 2 underwent FT in both modalities and PL only in fPACT owing to hearing difficulties in the MRI scanner. Participant 2 had difficulties in performing the other tasks. The authors affirm that the human research participants provided written informed consent for publication of the retinal images and potentially identifiable information in Fig. 2 and Supplementary Video 3 and the 'Participants' section.

Protocols. For fPACT stimuli, a participant lay on a height-adjustable bed with two stereo speakers placed on both sides of the head. During fMRI, stimuli were presented through a 7-T-compatible earphone system (S15, Sensimetrics). Both

fPACT and fMRI shared the same auditory cues. The auditory cues used a short rising tone beep as the start of a stimulus and a falling tone beep as the end. The participants were pretrained and imaged with one or more of the following stimuli: FT, LP, TT, LP and WG. Stimulation paradigms are provided in Supplementary Fig. 6.

Reporting Summary. Further information on research design is available in the Nature Research Reporting Summary linked to this article.

Data availability

The main data supporting the results in this study are available within the paper and its Supplementary Information. 3D functional image stacks of fMRI and fPACT for participant 3 (FT and LP session 1) are available online (https://doi.org/10.5061/dryad.sxksn0310). Other data are too large to be publicly shared, yet they are available for research purposes from the corresponding authors on reasonable request.

Code availability

The fMRI data were processed using the freely available software package SPM12. The codes used to extract the fPACT function are available online (https://doi.org/10.5281/zenodo.4615721). The reconstruction codes based on the universal backprojection algorithm, the system control software and the data collection software are proprietary and used in licensed technologies, yet they are available from the corresponding authors on reasonable request.

References

1. Logothetis, N. K. What we can do and what we cannot do with fMRI. *Nature* **453**, 869–878 (2008).
2. Ogawa, S., Lee, T.-M., Kay, A. R. & Tank, D. W. Brain magnetic resonance imaging with contrast dependent on blood oxygenation. *Proc. Natl Acad. Sci. USA* **87**, 9868–9872 (1990).
3. Pfeuffer, J. et al. Zoomed functional imaging in the human brain at 7 Tesla with simultaneous high spatial and high temporal resolution. *Neuroimage* **17**, 272–286 (2002).
4. Nowogrodzki, A. The world's strongest MRI machines are pushing human imaging to new limits. *Nature* **563**, 24–26 (2018).
5. Schenck, J. F. The role of magnetic susceptibility in magnetic resonance imaging: MRI magnetic compatibility of the first and second kinds. *Med. Phys.* **23**, 815–850 (1996).
6. Price, D. L., De Wilde, J. P., Papadaki, A. M., Curran, J. S. & Kitney, R. I. Investigation of acoustic noise on 15 MRI scanners from 0.2 T to 3 T. *J. Magn. Reson. Imaging* **13**, 288–293 (2001).
7. Rahmim, A. & Zaidi, H. PET versus SPECT: strengths, limitations and challenges. *Nucl. Med. Commun.* **29**, 193–207 (2008).
8. Darvas, F., Pantazis, D., Kucukaltun-Yildirim, E. & Leahy, R. M. Mapping human brain function with MEG and EEG: methods and validation. *NeuroImage* **23**, S289–S299 (2004).
9. Eggebrecht, A. T. et al. Mapping distributed brain function and networks with diffuse optical tomography. *Nat. Photon.* **8**, 448–454 (2014).
10. Demene, C. et al. Functional ultrasound imaging of brain activity in human newborns. *Sci. Transl. Med.* **9**, eaah6756 (2017).
11. Wang, X. et al. Noninvasive laser-induced photoacoustic tomography for structural and functional in vivo imaging of the brain. *Nat. Biotechnol.* **21**, 803–806 (2003).
12. Wang, L. V. & Hu, S. Photoacoustic tomography: in vivo imaging from organelles to organs. *Science* **335**, 1458–1462 (2012).
13. Li, L. et al. Single-impulse panoramic photoacoustic computed tomography of small-animal whole-body dynamics at high spatiotemporal resolution. *Nat. Biomed. Eng.* **1**, 0071 (2017).
14. Wray, P., Lin, L., Hu, P. & Wang, L. V. Photoacoustic computed tomography of human extremities. *J. Biomed. Opt.* **24**, 026003 (2019).
15. Lin, L. et al. Single-breath-hold photoacoustic computed tomography of the breast. *Nat. Commun.* **9**, 2352 (2018).
16. Jathoul, A. P. et al. Deep in vivo photoacoustic imaging of mammalian tissues using a tyrosinase-based genetic reporter. *Nat. Photon.* **9**, 239–246 (2015).
17. Wu, Z. et al. A microrobotic system guided by photoacoustic computed tomography for targeted navigation in intestines in vivo. *Sci. Robot.* **4**, eaax0613 (2019).
18. Lin, H.-C. A. et al. Ultrafast volumetric optoacoustic imaging of whole isolated beating mouse heart. *Sci. Rep.* **8**, 14132 (2018).
19. Nasiriavanaki, M. et al. High-resolution photoacoustic tomography of resting-state functional connectivity in the mouse brain. *Proc. Natl Acad. Sci. USA* **111**, 21–26 (2014).
20. Gottschalk, S. et al. Rapid volumetric optoacoustic imaging of neural dynamics across the mouse brain. *Nat. Biomed. Eng.* **3**, 392–401 (2019).
21. Ravina, K. et al. Prospects of photo-and thermoacoustic imaging in neurosurgery. *Neurosurgery* **87**, 11–24 (2020).
22. Nie, L. et al. Photoacoustic tomography through a whole adult human skull with a photon recycler. *J. Biomed. Opt.* **17**, 110506 (2012).
23. Xiang, L., Wang, B., Ji, L. & Jiang, H. 4-D photoacoustic tomography. *Sci. Rep.* **3**, 1113 (2013).
24. Deán-Ben, X. L. et al. Functional optoacoustic neuro-tomography for scalable whole-brain monitoring of calcium indicators. *Light Sci. Appl.* **5**, e16201 (2016).
25. Deán-Ben, X. L., Fehm, T. F., Ford, S. J., Gottschalk, S. & Razansky, D. Spiral volumetric optoacoustic tomography visualizes multi-scale dynamics in mice. *Light Sci. Appl.* **6**, e16247 (2017).
26. Matsumoto, Y. et al. Visualising peripheral arterioles and venules through high-resolution and large-area photoacoustic imaging. *Sci. Rep.* **8**, 14930 (2018).
27. Fischl, B. & Dale, A. M. Measuring the thickness of the human cerebral cortex from magnetic resonance images. *Proc. Natl Acad. Sci. USA* **97**, 11050–11055 (2000).
28. Kern, M., Bert, S., Glanz, O., Schulze-Bonhage, A. & Ball, T. Human motor cortex relies on sparse and action-specific activation during laughing, smiling and speech production. *Commun. Biol.* **2**, 118 (2019).
29. Friston, K. J. et al. Statistical parametric maps in functional imaging: a general linear approach. *Hum. Brain Mapp.* **2**, 189–210 (1994).
30. Strangman, G., Culver, J. P., Thompson, J. H. & Boas, D. A. A quantitative comparison of simultaneous BOLD fMRI and NIRS recordings during functional brain activation. *Neuroimage* **17**, 719–731 (2002).
31. Pujol, J., Deus, J., Losilla, J. M. & Capdevila, A. Cerebral lateralization of language in normal left-handed people studied by functional MRI. *Neurology* **52**, 1038–1038 (1999).
32. Brown, S., Ngan, E. & Liotti, M. A larynx area in the human motor cortex. *Cereb. Cortex* **18**, 837–845 (2008).
33. Price, C. J. The anatomy of language: a review of 100 fMRI studies published in 2009. *Ann. N. Y. Acad. Sci.* **1191**, 62–88 (2010).
34. American National Standards Institute *American National Standard for the Safe Use of Lasers* ANSI z136.1–2007 (Laser Institute of America, 2007).
35. Zhang, D. & Raichle, M. E. Disease and the brain's dark energy. *Nat. Rev. Neurol.* **6**, 15–28 (2010).
36. Na, S. et al. Transcranial photoacoustic computed tomography based on a layered back-projection method. *Photoacoustics* **20**, 100213 (2020).
37. Shnaiderman, R. et al. A submicrometre silicon-on-insulator resonator for ultrasound detection. *Nature* **585**, 372–378 (2020).
38. Poudel, J., Na, S., Wang, L. V. & Anastasio, M. A. Iterative image reconstruction in transcranial photoacoustic tomography based on the elastic wave equation. *Phys. Med. Biol.* **65**, 055009 (2020).
39. Mitsuhashi, K. et al. A forward-adjoint operator pair based on the elastic wave equation for use in transcranial photoacoustic computed tomography. *SIAM J. Imaging Sci.* **10**, 2022–2048 (2017).
40. Javaherian, A. & Holman, S. A continuous adjoint for photo-acoustic tomography of the brain. *Inverse Probl.* **34**, 085003 (2018).
41. Guasch, L., Agudo, O. C., Tang, M.-X., Nachev, P. & Warner, M. Full-waveform inversion imaging of the human brain. *NPJ Digit. Med.* **3**, 28 (2020).
42. Ulyanov, D., Vedaldi, A. & Lempitsky, V. Deep image prior. In *Proc. IEEE Conference on Computer Vision and Pattern Recognition* (eds Mortensen, E. & Brendel, W.) 9446–9454 (IEEE, 2018).
43. Heckel, R. & Hand, P. Deep decoder: concise image representations from untrained non-convolutional networks. Preprint at https://arxiv.org/abs/1810.03982 (2018).
44. Bostan, E., Heckel, R., Chen, M., Kellman, M. & Waller, L. Deep phase decoder: self-calibrating phase microscopy with an untrained deep neural network. *Optica* **7**, 559–562 (2020).
45. He, Y., Shi, J., Maslov, K. I., Cao, R. & Wang, L. V. Wave of single-impulse-stimulated fast initial dip in single vessels of mouse brains imaged by high-speed functional photoacoustic microscopy. *J. Biomed. Opt.* **25**, 066501 (2020).
46. Hu, P., Li, L., Lin, L. & Wang, L. V. Spatiotemporal antialiasing in photoacoustic computed tomography. *IEEE Trans. Med. Imaging* **39**, 3535–3247 (2020).
47. Xu, Y., Wang, L. V., Ambartsoumian, G. & Kuchment, P. Reconstructions in limited-view thermoacoustic tomography. *Med. Phys.* **31**, 724–733 (2004).
48. Kedenburg, S., Vieweg, M., Gissibl, T. & Giessen, H. Linear refractive index and absorption measurements of nonlinear optical liquids in the visible and near-infrared spectral region. *Opt. Mater. Express* **2**, 1588–1611 (2012).
49. Ashburner, J. et al. *SPM12 Manual* (Wellcome Centre for Human Neuroimaging, Institute of Neurology, UCL, London, UK, 2014).

50. Landis, J. R. & Koch, G. G. The measurement of observer agreement for categorical data. *Biometrics* **33**, 159–174 (1977).

Author contributions
L.V.W., C.Y.L., S.N. and J.J.R. conceived the project. S.N., J.J.R., C.Y.L. and L.V.W. designed the study. L.L., S.N., K.M. and J.S. built the system hardware. S.N. developed the system software. S.N., X.Y. and J.J.R. performed the PACT experiments. K.B.J. and L.Y. performed the MRI experiments. P.H., X.Y. and S.N. developed the reconstruction algorithms. X.Y., S.N., K.B.J., J.J.R., C.Y.L., D.J.W. and L.V.W. analysed and interpreted the data. J.J.R. and C.Y.L. recruited the participants. S.N., J.J.R. and X.Y. wrote the manuscript with input from all of the authors. L.V.W., C.Y.L. and D.J.W. supervised the study.

Competing interests
L.V.W. has a financial interest in Microphotoacoustics Inc., CalPACT LLC and Union Photoacoustic Technologies Ltd., which, however, did not support this work. K.M. has a financial interest in Microphotoacoustics, Inc. The other authors declare no competing interests.

Additional information
Supplementary information The online version contains supplementary material available at https://doi.org/10.1038/s41551-021-00735-8.

Correspondence and requests for materials should be addressed to C.Y.L. or L.V.W.

Peer review information *Nature Biomedical Engineering* thanks the anonymous reviewers for their contribution to the peer review of this work.

Reprints and permissions information is available at www.nature.com/reprints.

Publisher's note Springer Nature remains neutral with regard to jurisdictional claims in published maps and institutional affiliations.

Corresponding author(s):   Lihong V. Wang

Last updated by author(s): Mar 20, 2021

Reporting Summary

Nature Research wishes to improve the reproducibility of the work that we publish. This form provides structure for consistency and transparency in reporting. For further information on Nature Research policies, see our Editorial Policies and the Editorial Policy Checklist.

Statistics

For all statistical analyses, confirm that the following items are present in the figure legend, table legend, main text, or Methods section.

n/a	Confirmed	
☐	☒	The exact sample size (n) for each experimental group/condition, given as a discrete number and unit of measurement
☐	☒	A statement on whether measurements were taken from distinct samples or whether the same sample was measured repeatedly
☐	☒	The statistical test(s) used AND whether they are one- or two-sided *Only common tests should be described solely by name; describe more complex techniques in the Methods section.*
☒	☐	A description of all covariates tested
☒	☐	A description of any assumptions or corrections, such as tests of normality and adjustment for multiple comparisons
☐	☒	A full description of the statistical parameters including central tendency (e.g. means) or other basic estimates (e.g. regression coefficient) AND variation (e.g. standard deviation) or associated estimates of uncertainty (e.g. confidence intervals)
☐	☒	For null hypothesis testing, the test statistic (e.g. F, t, r) with confidence intervals, effect sizes, degrees of freedom and P value noted *Give P values as exact values whenever suitable.*
☒	☐	For Bayesian analysis, information on the choice of priors and Markov chain Monte Carlo settings
☒	☐	For hierarchical and complex designs, identification of the appropriate level for tests and full reporting of outcomes
☐	☒	Estimates of effect sizes (e.g. Cohen's d, Pearson's r), indicating how they were calculated

Our web collection on statistics for biologists contains articles on many of the points above.

Software and code

Policy information about availability of computer code

Data collection	Python 3.7.0, LabVIEW 2018 (National Instruments, Corp.), and MATLAB 2018b (MathWorks, Inc.). The system control software and the data collection software are proprietary and used in licensed technologies, yet they are available from the corresponding authors on reasonable request.
Data analysis	Python 3.7.0, MATLAB 2018b, and SPM12. The codes used to extract the fPACT function are available at https://doi.org/10.5281/zenodo.4615721. The universal backprojection algorithm was implemented in C++ with GPU acceleration. The reconstruction codes based on the universal backprojection algorithm are proprietary and used in licensed technologies, yet they are available from the corresponding authors on reasonable request.

For manuscripts utilizing custom algorithms or software that are central to the research but not yet described in published literature, software must be made available to editors and reviewers. We strongly encourage code deposition in a community repository (e.g. GitHub). See the Nature Research guidelines for submitting code & software for further information.

Data

Policy information about availability of data

All manuscripts must include a data availability statement. This statement should provide the following information, where applicable:
- Accession codes, unique identifiers, or web links for publicly available datasets
- A list of figures that have associated raw data
- A description of any restrictions on data availability

The main data supporting the results in this study are available within the paper and its Supplementary Information. 3D functional image stacks of fMRI and fPACT for Subject 3 (FT and LP session 1) are available at https://doi.org/10.5061/dryad.sxksn0310. Other data are too large to be publicly shared, yet they are available for research purposes from the corresponding authors on reasonable request.

Field-specific reporting

Please select the one below that is the best fit for your research. If you are not sure, read the appropriate sections before making your selection.

☒ Life sciences   ☐ Behavioural & social sciences   ☐ Ecological, evolutionary & environmental sciences

For a reference copy of the document with all sections, see nature.com/documents/nr-reporting-summary-flat.pdf

Life sciences study design

All studies must disclose on these points even when the disclosure is negative.

Sample size	The scope of this work was technology development. We used MRI results as the gold standard to verify the functional results of the proposed PACT technology. We recruited four subjects, who underwent multiple tasks in multiple sessions. In total, there were 34 datasets for verifying the effectiveness of the proposed technology.
Data exclusions	No data were excluded from the study.
Replication	The reproducibility of the findings was evaluated via repeated measurements. For fPACT, we imaged Subject 1 three times for each of the functional tasks, including finger tapping (FT), lip puckering (LP), tongue tapping (TT), passive listening (PL), and silent word generation (WG). We imaged Subject 2 once for FT, LP, TT, PL and WG. We imaged Subject 3 twice for FT, LP, TT, PL and WG. We imaged Subject 4 twice for FT and PL. For gold-standard fMRI, we imaged Subjects 1 and 2 once for FT, LP, TT, PL and WG. We imaged Subjects 3 and 4 once for FT. The fMRI measurements were performed about 3 hours after the first fPACT sessions for each subject. The time between each two successive fPACT sessions was one week for each subject. The reproducibility was externally verified by comparing the repeated fPACT results with the gold-standard fMRI results. The reproducibility was Internally verified among repeated measurements. Metrics of dice coefficient, spatial correlation, and center-of-mass error were used.
Randomization	Although required with clinically intact neurologic exams and completely healed surgical wounds, participants were randomly recruited to join the study.
Blinding	The investigators were blinded to group allocation during data collection and analysis.

Reporting for specific materials, systems and methods

We require information from authors about some types of materials, experimental systems and methods used in many studies. Here, indicate whether each material, system or method listed is relevant to your study. If you are not sure if a list item applies to your research, read the appropriate section before selecting a response.

Materials & experimental systems

n/a	Involved in the study
☒	☐ Antibodies
☒	☐ Eukaryotic cell lines
☒	☐ Palaeontology and archaeology
☒	☐ Animals and other organisms
☐	☒ Human research participants
☒	☐ Clinical data
☒	☐ Dual use research of concern

Methods

n/a	Involved in the study
☒	☐ ChIP-seq
☒	☐ Flow cytometry
☐	☒ MRI-based neuroimaging

Human research participants

Policy information about studies involving human research participants

Population characteristics	Four adult male post-hemicraniectomy patients (Subject 1: left hemicraniectomy, aged 34, not Hispanic or Latino; Subject 2: left hemicraniectomy, aged 25, Latino; Subject 3: right hemicraniectomy, aged 19, not Hispanic nor Latino; Subject 4: right hemicraniectomy, aged 41, Latino) with clinically intact neurologic exams and completely healed surgical wounds were recruited.
Recruitment	Participants were recruited from the Rancho Los Amigos National Rehabilitation Center. Participants were informed with the study contents by collaborating physicians during clinical visits. All subjects who were interested in this study could participate as long as they passed clinically intact neurologic exams and had completely healed surgical wounds.
Ethics oversight	The study was approved by the institutional review boards of the California Institute of technology, the University of Southern California, and the Rancho Los Amigos National Rehabilitation Center.

Note that full information on the approval of the study protocol must also be provided in the manuscript.

Magnetic resonance imaging

Experimental design

Design type	Tasks were block-designed, and included finger tapping, lip puckering, tongue tapping, passive story listening, and silent word generation.
Design specifications	The design specifications are described in the Supplementary information.
Behavioral performance measures	Subjects were familiarized with the tasks before undergoing experiments, and were encouraged to report issues regarding performing tasks. Except for Subject 4, who reported difficulties in hearing the commands in fMRI during passive listening, no other issues were reported.

Acquisition

Imaging type(s)	Functional and structural images were acquired.
Field strength	7 Tesla
Sequence & imaging parameters	Sequence and imaging parameters are reported in Methods.
Area of acquisition	Whole brain

Diffusion MRI   ☐ Used   ☒ Not used

Preprocessing

Preprocessing software	The fMRI data were pretreated with motion correction, spatial smoothing (3-mm FWHM Gaussian kernel), and temporal filtration (0.01-Hz high pass) before being analysed by the GLM in SPM12.
Normalization	The data were not normalized because each data set was individually compared with the fPACT results.
Normalization template	The data were not normalized.
Noise and artifact removal	Motion correction using least squares rigid-body registration in SPM12.
Volume censoring	Based on the performance measures, no volume censoring was performed.

Statistical modeling & inference

Model type and settings	Functional data were analysed using the GLM, and significance of regression coefficients were computed using Student's t-test. Goodness of fit of the GLM model was assessed with F-test. Agreement between fMRI and fPACT results were assessed using dice coefficient, spatial correlation, temporal correlation, and center-of-mass error.
Effect(s) tested	Generic tasks were defined: tapping finger, puckering lip, tapping tongue, listening to story, generating word based on starting words vs. baseline.

Specify type of analysis: ☒ Whole brain   ☐ ROI-based   ☐ Both

Statistic type for inference (See Eklund et al. 2016)	Voxel-wise
Correction	Statistical thresholds noted throughout and FDR.

Models & analysis

n/a	Involved in the study
☒	☐ Functional and/or effective connectivity
☒	☐ Graph analysis
☒	☐ Multivariate modeling or predictive analysis